Martensitic transformation induced strength-ductility synergy in additively manufactured maraging 250 steel by thermal history engineering

Shahryar Mooraj [a,1], Shuai Feng [a,1], Matthew Luebbe [b], Matthew Register [c], Tianyi Li [d], Baris Yavas [e], David P. Schmidt [a], Matthew W. Priddy [c], Marc Pepi [f], Michael B. Nicholas [f], Victor K. Champagne [f], Mark Aindow [e], Haiming Wen [b], Wen Chen [a, *]

[a] Department of Mechanical and Industrial Engineering, University of Massachusetts Amherst, Amherst, MA, 01003, USA

[b] Department of Materials Science and Engineering, Missouri University of Science and Technology, Rolla, MO, 65409, USA

[c] Department of Mechanical Engineering, Mississippi State University, Mississippi State, MS, 39759, USA

[d] X-ray Science Division, Argonne National Laboratory, Argonne, IL 60439, USA

[e] Department of Materials Science and Engineering & Institute of Materials Science, University of Connecticut, 97 North Eagleville Rd. Unit 3136, Storrs, CT 06269, United States

[f] U.S. Army Research Laboratory, Aberdeen Proving Ground, Adelphi, MD, 21005, USA

[*] Corresponding author. E-mail address: wenchen@umass.edu

[1] These authors contributed equally to this work.

Abstract

Maraging steels are known for their exceptional strength but suffer from limited work hardening and ductility. Here, we report an intermittent printing approach to tailor the microstructure and mechanical properties of maraging 250 steel via engineering of the thermal history during plasma arc additive manufacturing (PAAM). Through introducing a dwell time between adjacent layers, the maraging 250 steel is cooled below the martensite start temperature, triggering a thermally driven, in-situ martensitic transformation during the printing process. Re-heating or thermal cycling during subsequent layer deposition impedes complete martensitic transformation, enabling coexistence of martensite and retained austenite phases with elemental segregation. The enrichment of Ni in the austenite phase promotes stabilization of the retained austenite upon cooling down to room temperature. The retained austenite is yet metastable during deformation, leading to stress-induced martensitic transformation under loading. Specifically, a 3 min interlayer dwell time produces a maraging 250 steel with approximately 8% retained austenite, resulting in improved work hardening via martensitic transformation induced plasticity (TRIP) during deformation. Meanwhile, the higher cooling rate induced by the dwell time results in substantially refined grain structures with an increased dislocation density, leading to a simultaneously improved yield strength. Notably, the yield strength increases from 836 MPa (0 min dwell) to 990 MPa (3 min dwell), and the uniform elongation increases from 3.2% (0 min dwell) to 6.5% (3 min dwell). This intermittent deposition strategy demonstrates the potential to tune the microstructure and mechanical properties of maraging steels through engineering the thermal history during additive manufacturing.

Keywords: Additive manufacturing; maraging steel; mechanical properties; martensitic transformation; thermal history

1. Introduction

Maraging steels are a critical class of alloys for many structural applications such as aircraft construction, submarine hulls, tooling, and molding [1–4]. These steels typically show a high Ni content, which stabilizes the austenite phase and prevents the formation of ferrite upon solidification [5,6]. During cooling, the metastable face-centered cubic (FCC) austenite phase can transform into BCC martensite [7]. Maraging steels are well known for their excellent mechanical properties, particularly high strength (> 1GPa) due to the presence of a lath body-centered cubic (BCC) martensite matrix [8,9]. Despite their high yield strength, maraging steels often show limited work hardening and thus tend to exhibit necking almost immediately after yielding under tensile testing [10]. This weak work hardening is rooted in the limited capability of intragranular dislocation multiplication of the BCC martensite during plastic deformation as the BCC phase does not have close packed slip planes and requires high flow stresses to activate dislocation motion [11,12]. The combination of the high yield strength and low uniform elongation also makes traditional thermo-mechanical processing of maraging steels a significant challenge. For example, typical forging of maraging steels to achieve desired application dimensions must be carried out at elevated temperatures of up to 1000 ℃, making the process highly cumbersome and expensive [13].

Additive manufacturing (AM) offers a unique means to fabricate net-shaped components with non-equilibrium microstructures that are not readily accessible by conventional manufacturing approaches such as casting [14–17]. The solidification microstructure and mechanical properties of additively manufactured alloys are highly dependent on the cooling rate and thermal history during AM [18–23]. Among AM technologies, plasma arc additive manufacturing (PAAM) enables production of large-scale parts with significant savings in costs and time over laser-based AM techniques such as powder-bed fusion (PBF) or directed energy deposition (DED) [24]. In PAAM, a large high-frequency voltage is built up between a tungsten electrode and a plasma torch nozzle that initiates an arc between the two. An inert gas like argon flows to the torch tip and becomes an ionized plasma directed towards the substrate. The plasma in the nozzle creates a path for a lower voltage arc with a large constant current to initiate between the torch and substrate. This arc is referred to as the main arc. Then, feedstock wire is fed into the plasma arc, melted, and deposited onto the substrate to achieve layer-by-layer deposition. A separate stream of argon from the plasma gas acts as a shielding gas to protect the melt pool from oxidation [25]. The large heat input during PAAM can cause severe heat accumulation in lower layers as the part may not completely cool before the deposition of the subsequent layers. In particular, this heat accumulation can induce large residual stresses in the as-printed part [26]. The increased thermal build-up also results in a lower cooling rate, leading to microstructural coarsening and degraded mechanical properties [27–29]. Furthermore, the printed maraging steels by PAAM often show an almost fully BCC martensitic structure with poor work hardening and tensile ductility [30].

In this work, an intermittent printing strategy with a dwell-time between adjacent layers is introduced to mitigate the severe heat accumulation during PAAM of maraging 250 steel. This dwell time is used to allow the previously deposited layers to cool, thus enabling a higher cooling rate in the overall part. The addition of this dwell-time results in a controlled thermal history where the temperature in the deposited layer is allowed to drop below the martensite start (M_s) temperature and is subsequently re-heated before the temperature reaches the martensite finish (M_f) temperature. Through precisely tailoring the thermal history in this manner, the martensitic transformation remains incomplete during printing, and the martensite and austenite phases can coexist. The coexistence of the two phases during printing enables the redistribution of Ni between the austenite and martensite phases. The enrichment of Ni in the austenite phase promotes stabilization of the retained austenite upon cooling down to room temperature. Such retained austenite is yet metastable during deformation, a feature that helps enhance the work hardening and tensile ductility of

the printed maraging 250 steel via martensitic transformation induced plasticity (TRIP) under loading. Meanwhile, the higher cooling rate by adding a dwell time also results in remarkably refined grain structures with an increased dislocation density, leading to a higher yield strength. The intermittent deposition strategy during PAAM allows us to achieve an outstanding strength-ductility synergy that outperforms conventional wrought and other additively manufactured maraging steel counterparts. This work suggests that engineering the thermal history to tune the microstructure and phase transformation pathway presents new opportunities to design additively manufactured maraging steels with improved mechanical performance.

2. Materials and Methods

2.1 Material fabrication

The PAAM system consists of a welding torch body attached to a large gantry system controlled by Aerotech drivers and software. Maraging 250 steel wire was used as a feedstock material and remotely fed under the PAAM electrode to coincide with the plasma arc during printing. Before printing bulk samples, 12 single tracks were printed as a preliminary study to identify optimized printing parameters (see Fig. 2 later). The optimized printing parameters were set as: welding voltage 30 V, current 182 A, welding speed 3 mm/s and wire feed speed 50 mm/s. During printing, ultrahigh purity argon was used as both the welding gas and the shielding gas. Using these parameters, thin walls of $80\ \text{mm} \times 10\ \text{mm} \times 20\ \text{mm}$ with a layer thickness of 1.2 mm were printed with different interlayer dwell times of 0 min, 1min, and 3 min to study the effects of different thermal histories on the microstructure and mechanical properties of the printed maraging 250 steel.

2.2 Mechanical testing

Tensile dog-bone samples were cut by wire electric discharge machining with a gauge dimension of 2 mm (width) × 1.5 mm (thickness) × 6.5 mm (length). Uniaxial tension tests were carried out at a strain rate of $2 \times 10^{-4}\ s^{-1}$ on an Instron 5969 machine with a built-in laser extensometer to precisely measure the strain. The tensile specimens were polished using 400, 800, and 1200 grit SiC abrasive papers prior to testing. All tension tests in this work were carried out parallel to the plasma arc scan direction.

2.3 Microstructural characterization

The microstructures of as-printed samples were studied by optical microscope (OM, OLYMPUS SC50) and electron backscatter diffraction (EBSD). EBSD was performed using a Helios Dual-Beam Nanolab scanning electron microscope operating at 30 kV with a scanning step size of 200 nm. The cross-sections of the samples were polished using SiC abrasive papers, followed by 20 nm oxide polishing suspension (OPS). Samples were electrochemically etched using a solution of 10% nitric acid and 90% ethanol at 0.6 V for 5 seconds. ImageJ was used to quantify the porosity of the as-printed samples and gas pycnometry measurements of these samples revealed that the porosity of all the samples were below 0.5%. Transmission electron microscopy (TEM) was used to investigate nanoscale microstructural features on a JEOL JEM 2100F system operated at 200 kV. Scanning transmission electron microscopy (STEM) was used in conjunction with energy dispersive X-ray spectroscopy (EDX) to measure the elemental segregation. TEM samples were prepared using focused ion beam (FIB) lift-out on the Helios. In-situ high-energy synchrotron X-ray diffraction (SXRD) was carried out at Argonne National Laboratory (ANL) at the 11-ID-C beamline to investigate the phase fraction in the as-printed samples as well as to explore the deformation mechanism under real-time tensile loading. The beam energy was set at 105.7 keV and the beam size was controlled by slits to maintain at 0.5 mm × 0.5 mm.

2.4 Thermal modeling

Using the Abaqus/Standard 2019 AM modeler plugin, two finite element thermal simulations were created for the 0 min and 3 min interlayer dwell times based on the as-printed part geometry. The heat transfer in the PAAM process is driven by the transient heat conduction equation below:

$$C_p \rho \frac{dT}{dt} = \frac{\delta}{\delta x}\left(k \frac{\delta T}{\delta x}\right) + \frac{\delta}{\delta y}\left(k \frac{\delta T}{\delta y}\right) + \frac{\delta}{\delta z}\left(k \frac{\delta T}{\delta z}\right) + q, \qquad (1)$$

where C_p is the specific heat capacity, ρ the density, T the temperature, k the thermal conductivity, and q the volumetric heat input. The thermal model utilizes a moving double ellipsoidal heat source defined by the Goldak heat source equation to simulate the arc power source [31]. The heat source includes two ellipsoidal shapes which are combined to simulate the different temperature gradients at the front and rear of the melt pool. Because of this separation of front and back, the temperature gradient fractions at the front (f_f) and at the rear (f_r) of the melt pool are used, where $f_f + f_r = 2$. The volumetric heat source equation for the power density of the front ellipsoid is:

$$q(x, y, z, t) = \frac{6\sqrt{3} P n f_f}{a_f b c \pi \sqrt{\pi}} exp\left(-3\frac{x^2}{a_f^2} - 3\frac{y^2}{b^2} - 3\frac{z^2}{c^2}\right), \qquad (2)$$

and the power density equation for the rear ellipsoid is similarly:

$$q(x, y, z, t) = \frac{6\sqrt{3} P n f_r}{a_r b c \pi \sqrt{\pi}} exp\left(-3\frac{x^2}{a_r^2} - 3\frac{y^2}{b^2} - 3\frac{z^2}{c^2}\right), \qquad (3)$$

where *q(x, y, z, t)* is the power density of the heat source, *P* the power input, *n* the efficiency of the arc, and *a*, *b*, and *c* the radii in the *x*, *y*, and *z* directions, respectively [31]. Goldak's heat source model was developed for arc welding applications and has since been used widely for many AM modeling efforts [32–37]. The heat source parameters used for the finite element thermal simulation were calibrated based on the experimentally measured bead widths and heights. The double ellipsoidal parameters and shape used for the two finite element thermal simulations can be found in Table 1 and Figure 1.

Table 1. The goldak heat source parameters used for the finite element thermal simulation.

Dwell Time	b	c	a_f	a_r	f_f	f_r
3 min	6.5	2.0	7.0	13.0	0.7	1.3
0 min	7.3	2.0	7.0	13.0	0.7	1.3

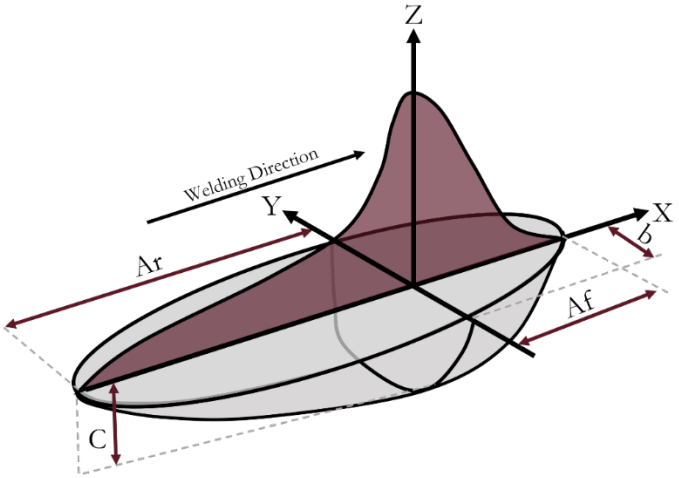

Fig. 1 Schematic illustration of the Goldak double ellipsoidal heat source shape used in the finite element thermal simulation.

3. Results

3.1 Process development

Printing defects such as keyhole pore, lack of fusion pores, and cracking are ubiquitous in metal additive manufacturing [38]. These printing defects can significantly degrade the properties of printed components [39–42]. Before printing multilayer bulk samples, an array of single tracks was printed with different processing parameters to explore the process window toward defect-free samples. The macrostructures of the deposited single tracks are shown in Fig. 2. The corresponding printing parameters used for these tracks are outlined in Supplementary Information Table S1. Tracks #1-6 were deposited at increasing scan speeds from 2 mm/s to 20 mm/s while under a constant voltage (29 V), current (165 A), and wire feed rate (50 mm/s). A higher scan speed results in less deposited material, which leads to a thinner track. The welding deposit becomes discontinuous in track #6 due to insufficient material feeding at an overhigh printing speed. Tracks #7-9 were printed at a higher voltage (30.5 V) and current (182 A) with increasing scan speeds from 5 mm/s to 12 mm/s. Again, the width of the tracks decreases with increasing the scan speed, accompanied by increased spattering. Previous studies have shown that spattering during plasma welding typically occurs due to strong penetration of the plasma into the working surface, which blows away molten metal at the edge of the melt pool [43].

The welding voltage and current were then further increased to 31.5 V and 195 A, respectively for tracks #10-12. As the scan speed increases from 5 mm/s (#10) to 12 mm/s (#12), the melt deposition shows a noticeable balling effect with significant spattering. Balling effect during wire-based welding or AM process is often associated with insufficient heat input as the temperature of the melt pool remains low [44]. The low temperature results in a high surface tension that prevents the melt pool from spreading out and leads to balling [44]. Thus, the heat input must be balanced to ensure sufficient melting to inhibit balling, while avoiding the over-penetration of the arc to prevent spattering. The optimal printing parameters were chosen based on the single track #7 which exhibits the most linear shape, consistent and reproducible thickness, and minimal spattering. After process optimization, multilayer thin walls with a layer thickness of 1.2 mm were printed using the printing conditions of track #7. Different interlayer dwell times of 0 min, 1 min, and 3 min were used to tune the thermal history and study their effects on solidification microstructures and material properties. Fig. 3 shows a representative thin wall deposition with 0 min dwell time between consecutive layers. The thin-wall sample exhibits a smooth surface and minimal spatter, making it suitable for further investigation.

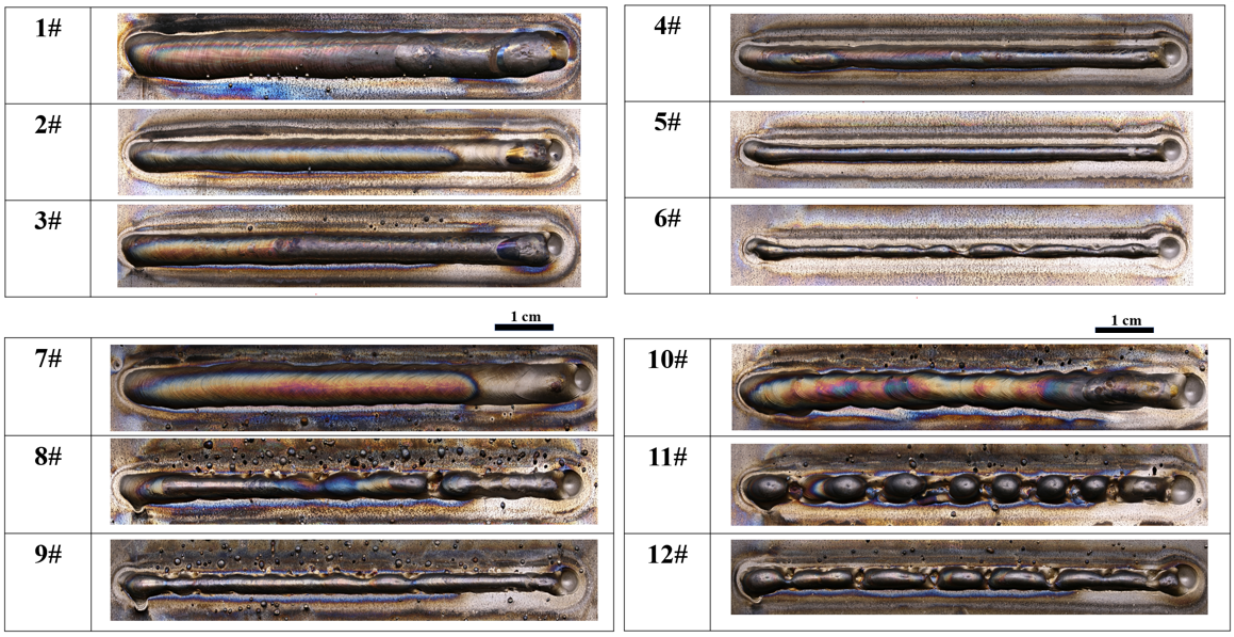

Fig. 2 Macrostructures of single tracks printed using different printing parameters. The printing parameters for each track are outlined in Supplementary Information Table S1.

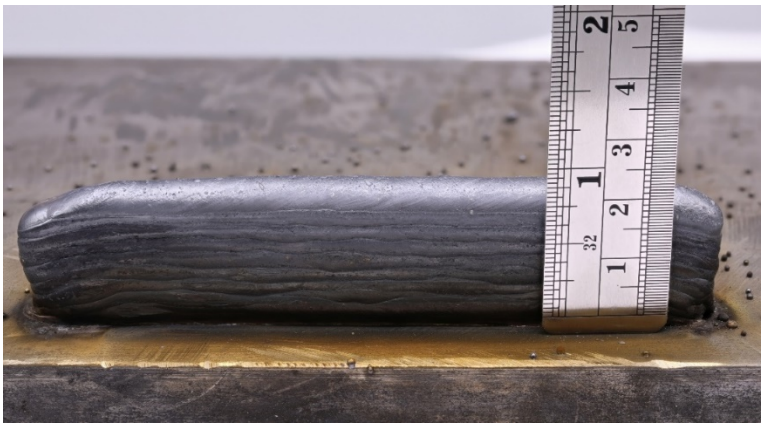

Fig. 3 A representative thin wall printed using processing parameters for single track #7.

3.2 Microstructural analysis

The purpose of this work is to study how tuning the thermal history can influence the solidification microstructure and mechanical properties of maraging 250 steel produced via PAAM. To this end, the printed thin walls were sectioned, polished, and etched to investigate the microstructural changes with different dwell times. Fig. 4 shows the optical micrographs of different samples with the build direction oriented vertically in the plane of the images. While gas pycnometry measurements of these samples reveal that the porosity of all the samples are below 0.5%, they show distinct microstructures. The 0 min and 1 min dwell samples appear a single-phase structure (Fig. 4a, b, d, and e). In contrast, the 3 min dwell sample (Fig, 4c and f) shows a significant phase contrast, suggesting there are different phases present. All the samples are featured by a columnar dendritic structure, which is typical for many metal alloys produced by AM techniques due to the strong thermal gradients along the build direction [45,46].

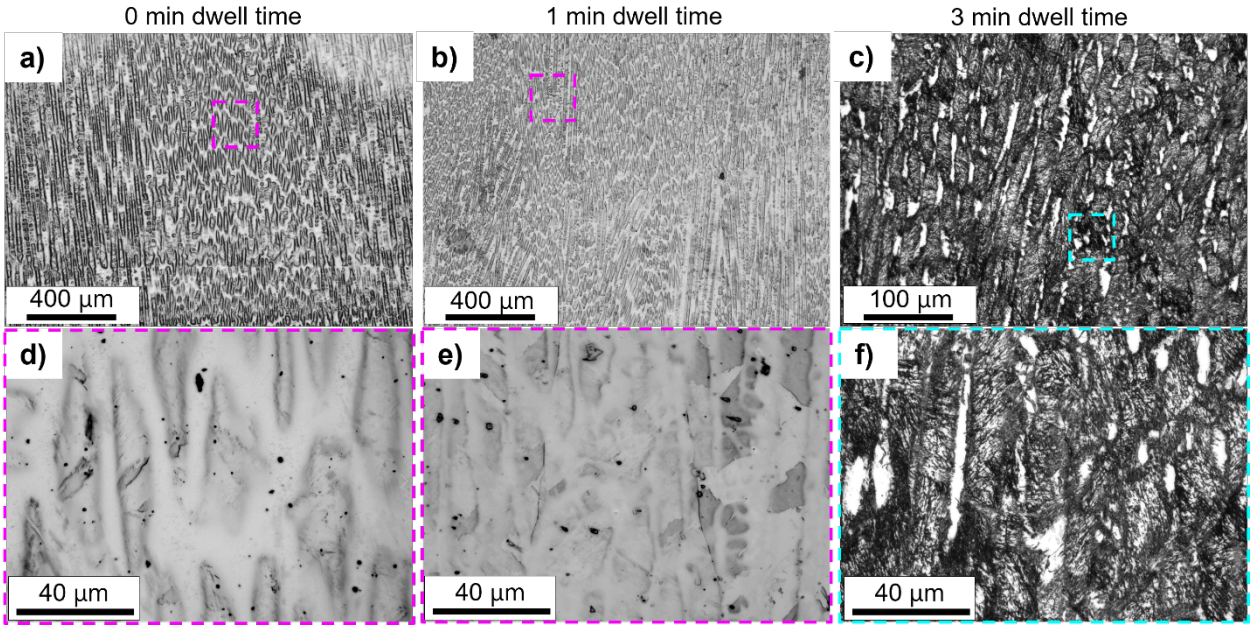

Fig. 4 Optical micrographs of as-printed samples with different dwell times between consecutive layers. (a) 0 min dwell time. (b) 1 min dwell time. (c) 3 min dwell time. (d-f) High magnification images of (a-c), respectively.

Due to the microstructural similarity between the 0 min and 1 min dwell samples, only the 0 min and 3 min dwell samples were further investigated by EBSD and TEM for comparison. Fig. 5 presents the inverse pole figure (IPF) maps, pole figures (PF), and multiple of uniform random distribution (MUD) of the 0 min and 3 min dwell samples. The MUD measures the relative intensity of a given crystallographic orientation compared to the expected intensity of a fully random texture. A higher MUD value implies a stronger crystallographic texture. The 0 min dwell sample shows a coarse and columnar grained structure with an average grain size of 82.6 µm (Fig. 5a). Fig. 5b shows the {100} PF of the 0 min sample with a high maximum MUD of 18.41, indicative of a strong <100> texture. Both the strong crystallographic texture and large grain size observed in the 0 min dwell sample result from the high thermal gradients across subsequent printed layers created by the deep penetration of the plasma arc that re-melts and heats previous layers. This strong thermal gradient induces epitaxial solidification growth of columnar grains along the build direction [47–50].

On the other hand, Fig. 5c shows that the 3 min dwell sample exhibits a substantially refined microstructure with an average grain size of 15.3 µm. Further, the 3 min dwell sample shows a much weaker <100> texture along the build direction compared to that in the 0 min dwell sample (Fig. 5d). Fig S1 illustrates the phase maps of both samples. The 0 min dwell sample appears to be fully BCC martensite while the 3 min dwell sample shows some minor FCC austenite inclusions. The presence of retained austenite as a secondary phase may disrupt the epitaxial growth of the martensite phase along the build direction, thus weakening the crystallographic texture in the 3 min dwell sample. Although the 3 min dwell sample shows apparently a minor inclusion of retained austenite (Fig. S1), it should be noted that the mechanical polishing process may induce stresses on the sample surface that lead to martensitic transformation in many retained austenite grains present on the surface [51]. Therefore, EBSD may underestimate the volume fraction of the retained austenite. To overcome this challenge, high-energy SXRD that can penetrate through a bulk volume was employed to precisely measure the phase constitute in the bulk sample, to be discussed in Section 3.3.

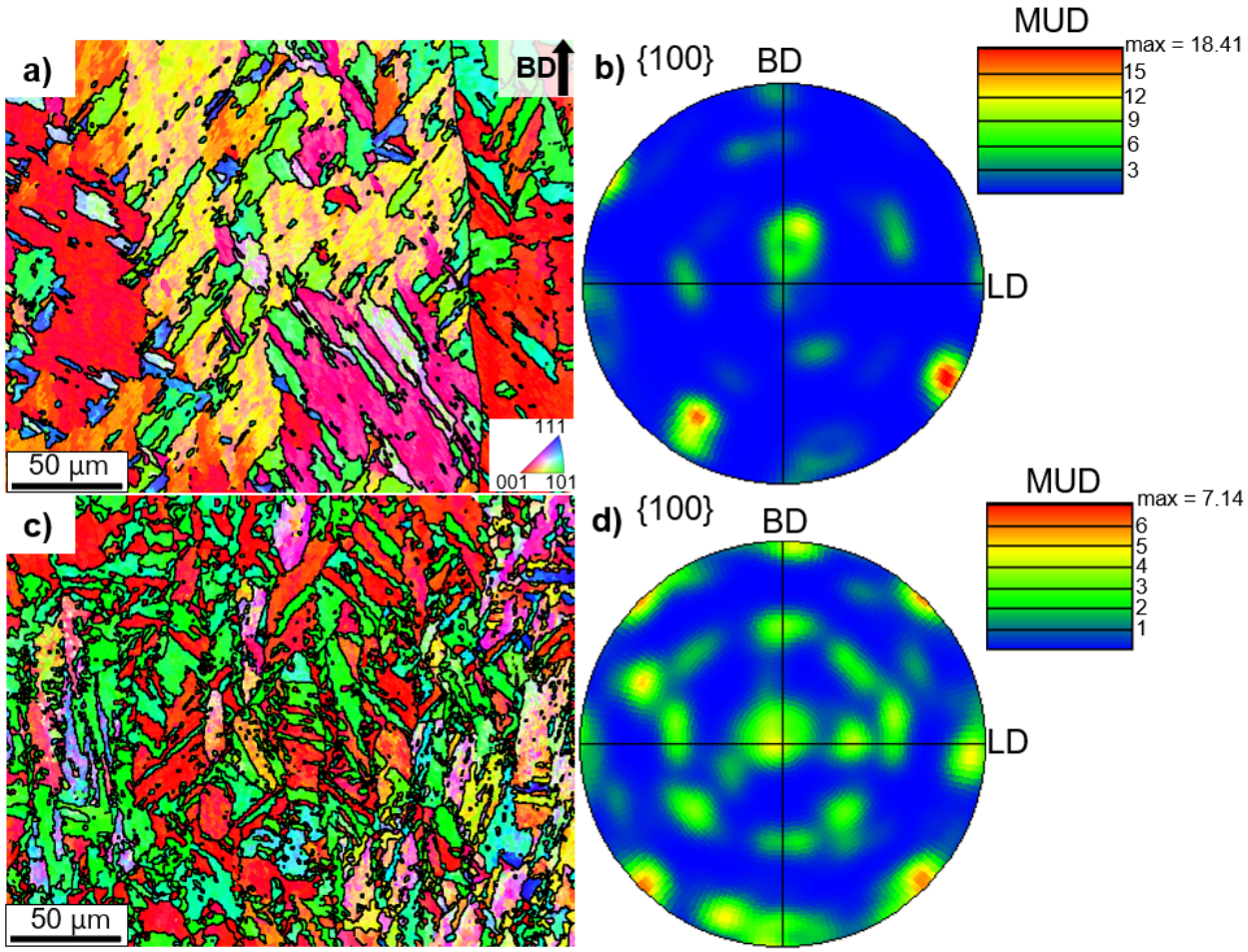

Fig. 5 EBSD data of the 0 min and 3 min dwell samples. (a) IPF map of the 0 min dwell sample, (b) {100} pole figure of the 0 min dwell sample together with the MUD result, (c) IPF map of the 3 min dwell sample, (d) {100} pole figure of the 3 min dwell sample together with the MUD result. The IPF legend in the bottom right corner of (a) applies to (c) as well.

We further examined the microstructures of the 0 min and 3 min dwell samples by TEM. Fig. 6 confirms that the 3 min dwell sample exhibits a more refined microstructure compared to the 0 min dwell sample. Selected-area electron diffraction (SAED) clearly reveals a fully single-phase BCC martensite structure in the 0 min dwell sample (Fig. 6a inset) while a dual-phase martensite and austenite structure in the 3 min dwell sample (Fig. 6b inset). These results are consistent with the prior EBSD results. Fig. 7a shows a STEM micrograph of the 3 min sample with an austenite grain labeled to explore the elemental segregation between the austenite and martensite phases. The white line indicates the scan path of STEM EDX measurement, and the yellow dotted box indicates the region where elemental mapping was carried out. Fig. 7b presents the elemental concentration of Ni and Mo measured along the white line in Fig. 7a. Notably, the concentration of Ni shows a peak within the austenite grain (labeled as γ). It is well known that Ni acts as a stabilizing element for austenite phase and reduces the martensite start (M_s) temperature [52]. Thus, Ni-enriched regions in the as-printed maraging 250 steel tend to increase the stability of the austenite phase, thereby deferring the martensitic transformation during cooling. This results in the formation of some retained austenite upon cooling down to room temperature. The elemental mapping of the yellow dotted box in Fig. 7a is shown in Fig. 7c. Here, we confirm that the austenite grain is rich in Ni and Mo compared to the surrounding martensite matrix. Such elemental segregation in the 3 min dwell sample is presumably

related to the incomplete martensitic transformation that allows for the elemental redistribution (or partitioning) between the martensite and retained austenite phases during printing. Such thermal-history-dependent phase transformation pathway will be discussed in detail in Section 4.3.

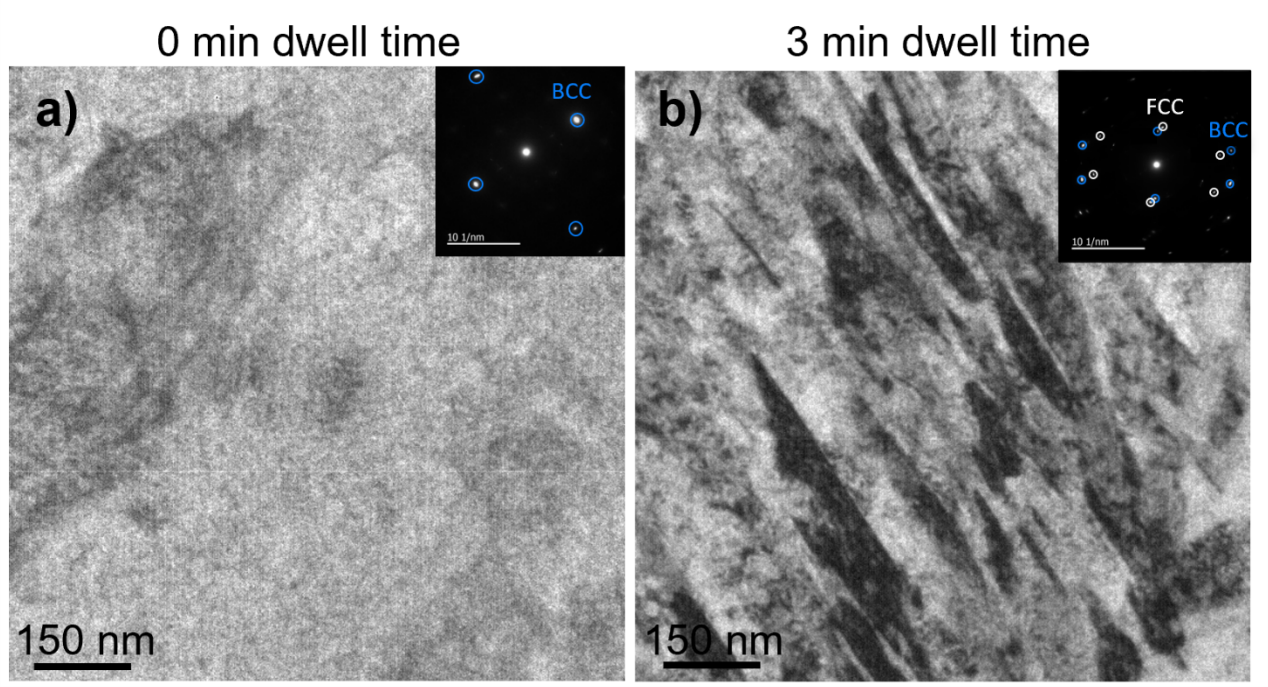

Fig. 6 TEM micrographs and SAED patterns of the 0 min and 3 min dwell samples. (a) TEM micrograph of the 0 min dwell sample, where the inset displays the SAED pattern. (b) TEM micrograph of the 3 min dwell, where the inset displays the SAED pattern.

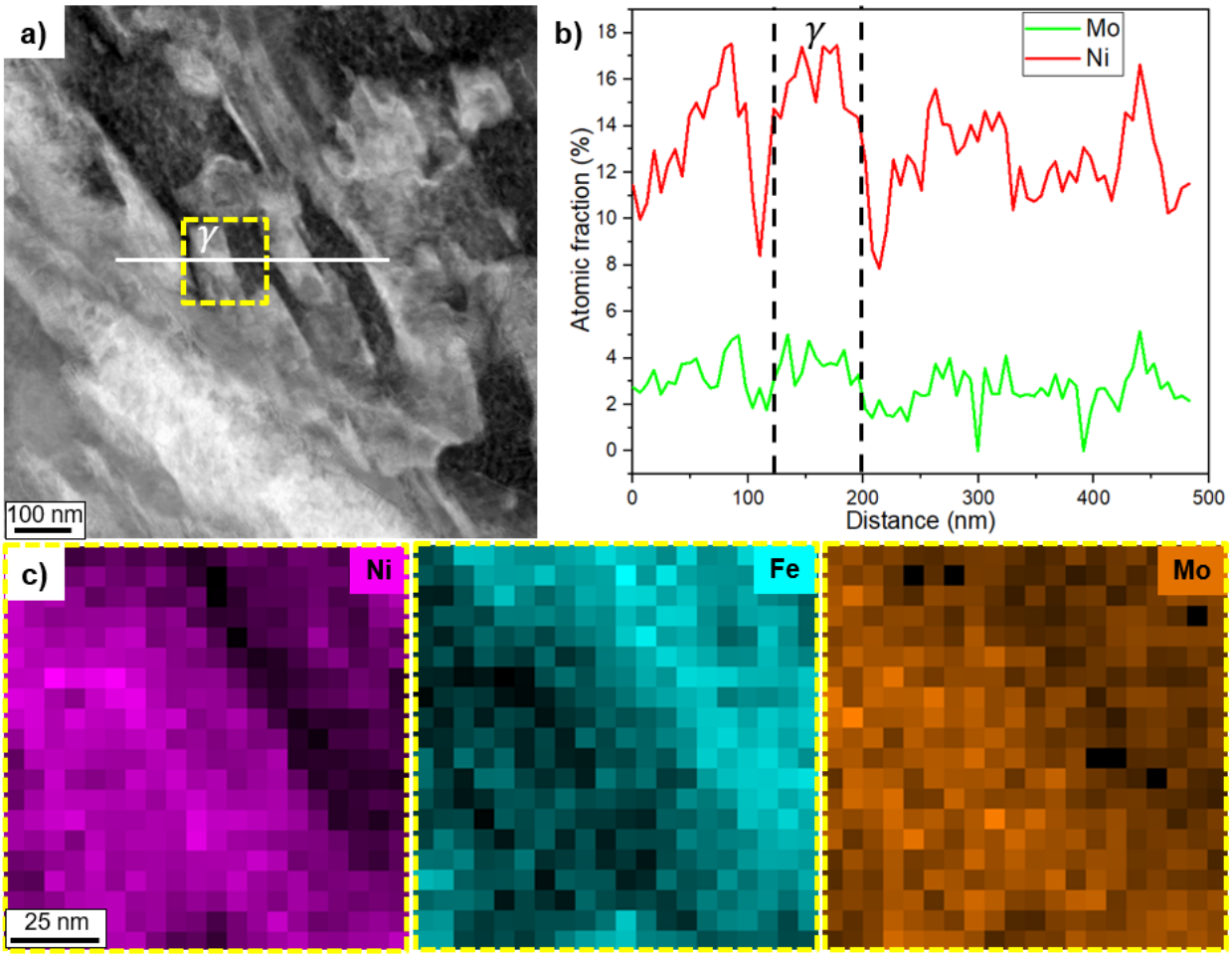

Fig. 7 STEM micrograph and STEM-EDX results of the 3 min dwell sample, showing chemical segregation between the austenite and martensite phases. (a) **S**TEM micrograph showing the EDX line scan and elemental mapping region which contains the austenite (γ) phase, (b) Atomic percent of Mo and Ni measured along the line scan, (c) Element maps of Ni, Fe, and Mo showing that the austenite phase is rich in Ni and Mo, compared to the martensite phase.

3.3 Mechanical properties and in situ SXRD patterns

Fig. 8a shows the tensile stress-strain curves of different samples in this study and the tensile properties are summarized in Table 2. Interestingly, the 3 min dwell sample shows simultaneously enhanced strength and uniform elongation with more sustained work-hardening compared to the 0 min and 1 min dwell samples. Specifically, the 3 min dwell sample exhibits remarkable increases in yield strength σ_y and ultimate tensile strength σ_{UTS} (990 MPa and 1250 MPa) compared to the 0 min (836 MPa and 1023 MPa) and 1 min (960 MPa and 1092 MPa) dwell samples. The 3 min dwell sample also shows an over two-fold increase in uniform elongation (6.5%) compared to the 0 min (3.2%) and 1 min (2.6%) dwell samples. In addition, the 3 min dwell sample exhibits a higher Young's modulus (164.9 GPa) compared to the 0 min (99.3 GPa) and 1 min (125.0 GPa) dwell samples. The simultaneous increases in σ_y, σ_{UTS}, and uniform elongation are surprising as most materials demonstrate a strength-ductility trade-off, yet the inclusion of the retained austenite breaks this commonly observed trade-off. The reason for this enhanced strength-ductility synergy will be discussed in detail in Sections 4.1 and 4.2.

To illustrate the exceptional strength-ductility synergy, we compare the tensile properties of the 3 min dwell sample with those of wrought and other maraging steel counterparts processed by wire arc additive manufacturing (WAAM) or laser powder-bed fusion (L-PBF). Fig. 8b shows that the 3 min dwell sample exhibits simultaneously enhanced yield strength and uniform elongation than maraging 250 steels processed by other methods [48,53,54]. The 3 min dwell sample even outperforms the L-PBF maraging 300 steels in terms of strength-ductility combination [9,55–62]. This result is particularly encouraging considering that maraging 300 steel contains a higher content of Co than maraging 250 steel, which typically results in increased strength and also material cost [63]. In addition to improved mechanical performance, it is worth noting that the wire feedstock material for PAAM is significantly cheaper than the powder feedstock material for L-PBF [64,65].

Fig. 9a and b present the in situ SXRD patterns of the 0 min and 3 min dwell samples at various strain levels during tensile deformation. Through Rietveld refinement of the diffraction patterns, it is seen that in the as-printed state no austenite is observed in the 0 min dwell sample while a volume fraction of 8% austenite is present in the 3 min dwell sample. However, we notice that the intensity of the austenite peaks of the 3 min dwell sample continuously decreases during deformation, indicating that the retailed austenite phase is metastable and undergoes a stress-induced martensitic phase transformation under loading. Meanwhile, the width of most diffraction peaks of both samples steadily increases during deformation, suggesting a continuously increased dislocation density. Section 4.1 will focus on comparing the deformation behavior of these two samples and in-depth peak line profile analysis will be utilized to unravel the mechanistic origin of their different mechanical properties.

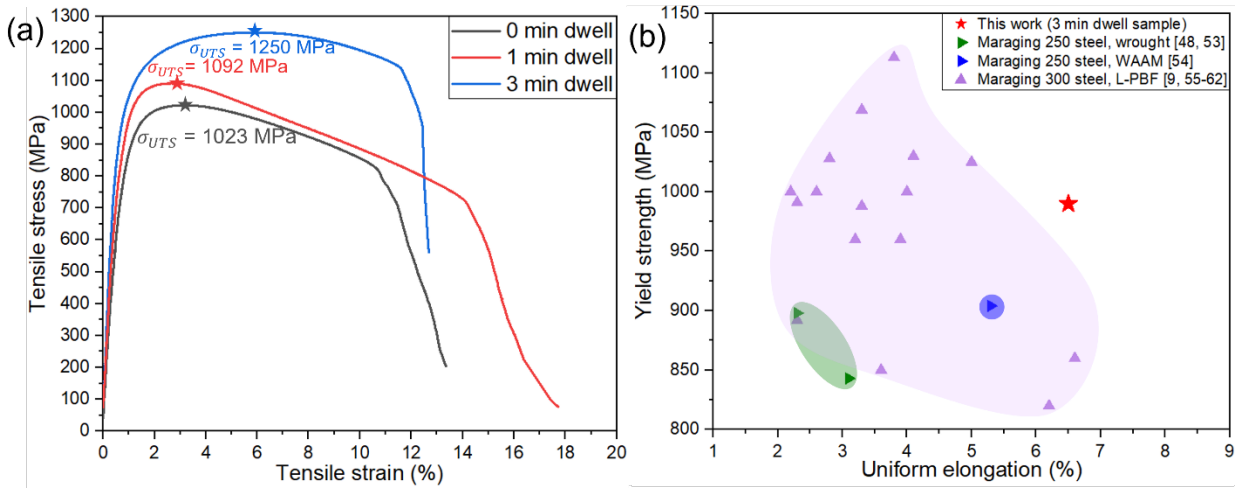

Fig. 8 Tensile properties of as-printed maraging 250 steel. (a) Tensile stress-strain curves of as-printed samples with different dwell times. (b) Comparison of tensile yield strength and uniform elongation of the 3 min dwell sample with those of wrought and WAAM maraging 250 steel and L-PBF maraging 300 steel [9,48,53–62].

Table 2 Tensile properties of the as-printed samples with different dwell times.

Dwell time	σ_{YS} (MPa)	σ_{UTS} (MPa)	Uniform Elongation (%)	Total Elongation (%)
0 min	836	1023	3.2	10.8
1 min	960	1092	2.6	14.1
3 min	990	1250	6.5	11.6

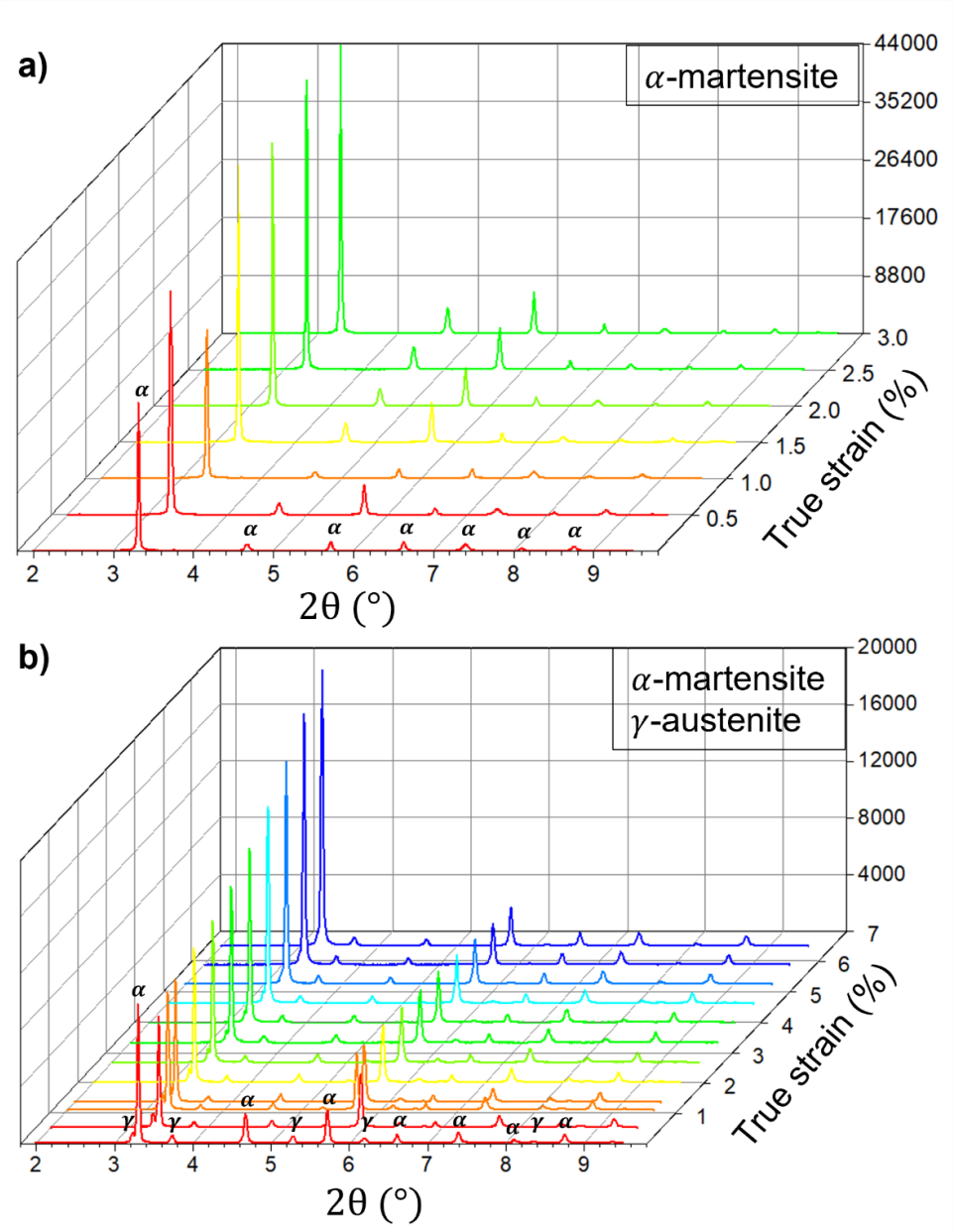

Fig. 9 In-situ synchrotron X-ray diffraction peak profiles of (a) 0 min dwell and (b) 3 min dwell samples during tensile deformation.

4. Discussion

4.1 In-situ synchrotron XRD analysis and deformation mechanism

In-situ SXRD can decipher stress partitioning between different crystallographic plane families and phases as well as quantify crystalline defect (e.g., dislocation) density evolution during deformation to provide mechanistic insight into the origin of the enhanced strength-ductility synergy for the 3 min dwell sample [19,66–68]. To reveal the deformation micro-mechanisms of the as-printed maraging 250 steel samples, analysis of the lattice strain as a function of true applied stress is performed. The lattice strain is calculated as:

$$\varepsilon_{hkl} = \frac{d_{hkl} - d_{hkl,0}}{d_{hkl,0}} \quad [1]$$

where ε_{hkl} is the strain of a specific lattice plane family $\{hkl\}$, d_{hkl} the d-spacing of that plane at a specific stress level, and $d_{hkl,0}$ the d-spacing of that plane under no load. Representative plane families in the 0 min and 3 min dwell samples are selected to depict the deformation micro-mechanism within each sample. Fig. 10a presents the lattice strain plots of the 0 min dwell sample. It is seen that all of the plane families exhibit a linear increase of lattice strain against the true stress when the macroscopic tensile stress-strain response is within the elastic regime. The slope of the macro-stress versus the lattice strain curves in the elastic region is referred to as the diffraction elastic constant (DEC), which is specific to each crystal orientation and reflects the inherent crystal anisotropy [69]. As the true stress increases, the strains of the {110} and {220} planes deviate from linearity and turn upwards as the stress approaches the macroscopic yield stress. Such a softening response indicates the onset of microyielding of these crystallographic plane families prior to macroyielding. Simultaneously, the {200} and {310} planes also deviate from linearity but turn downward. Such a stiffening response arises from the load shedding of the plastic {110} and {220} planes to the elastic {200} and {310} planes.

Fig. 10b shows the lattice strain plots of the BCC and FCC phases in the 3 min dwell sample. The lattice strains for the 3 min dwell sample show some kinks below 200 MPa. These kinks likely occur due to a combination of fitting error and residual stresses. The lattice strains of all planes in both phases initially follows a linear trend. Again, the different slopes of the macro-stress versus the lattice strain of different plane families arise from the inherent elastic anisotropy of a polycrystalline solid. As the true macroscopic stress increases the lattice planes in the BCC phase show a similar trend to those in the 0 min dwell sample, where the {200} plane carries more load while the {110} and {220} planes show a slight relaxation. This indicates the onset of microyielding of the {110} and {220} planes before macroyielding. From Fig. 10b, one can notice that the FCC-{220} shows significant microyielding and the FCC-{200} plane takes significantly higher load before macroyielding. The increase in the lattice strain of the FCC- {200} plane is even greater than that of the BCC-{200} plane, which suggests that the FCC experiences more load shedding between its plastic reflection ({220}) and elastic reflection ({200}).

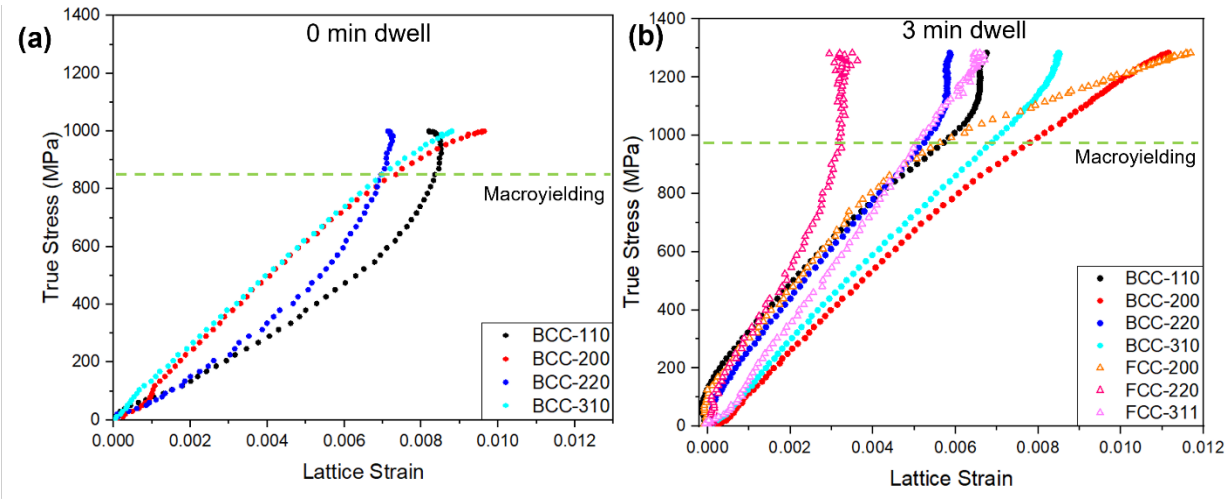

Fig. 10 In-situ evolution of lattice strain against macroscopic true stress in the as-printed samples during uniaxial tension. (a) Evolution of lattice strain for representative BCC crystallographic plane families in the 0 min dwell sample. (b) Evolution of lattice strain for representative crystallographic plane families of the BCC and FCC phases in the 3 min dwell sample.

In addition to the lattice strains, the stress partitioning between different phases in the 3 min dwell sample is also analyzed to investigate the contribution of each phase to the elastic/plastic deformation of the material. The stress within each phase is approximated based on the lattice strain via the Hooke's law [70]:

$$\sigma_{hkl} = E_{hkl} \cdot \varepsilon_{hkl} \quad [2]$$

where σ_{hkl} is the stress acting on the plane {hkl} and E_{hkl} is the DEC of the plane. The {211} plane in the BCC phase and the {311} plane in the FCC phase are used to represent the overall stress taken by each phase as these planes are least sensitive to intergranular strains [71,72]. The stress partitioning between different phases as well as the overall flow stress in the sample are shown in Fig. 11a. This figure illustrates that the FCC austenite phase exhibits higher strain hardening rates than the BCC martensite phase after macroscopic yielding. In order to understand the contribution of each phase in more detail, Rietveld refinement is also used to calculate phase fraction evolution during deformation. Fig. 11b displays the variation in the volume fraction of the FCC phase (i.e., retained austenite) as a function of the true applied strain. It is seen that the volume fraction of the retained austenite decreases continuously during plastic deformation, indicating the occurrence of dynamic martensitic transformation during deformation of the 3 min dwell sample. As the stress level approaches the UTS, the retained austenite almost completely diminishes and necking sets in subsequently. This result indicates that once the martensitic transformation is fully completed, the martensite phase can no longer offer sustained work hardening and necking instability follows. Therefore, the increase in the uniform elongation of the 3 min dwell sample is largely attributed to the stress-induced phase transformation from the retained austenite to martensite during deformation.

We further analyzed the dislocation density in different samples based on the modified Williamson-Hall method [73]. Fig. 11c illustrates the plot of the dislocation density (ρ) vs. the true applied strain for both samples. Initially, the BCC phases in the 0 min and 3 min dwell samples show a high dislocation density of approximately 2.5×10^{15} m^{-2} and 1.5×10^{15} m^{-2}, respectively. The FCC phase in the 3 min dwell sample shows an even higher dislocation density of 3.7×10^{15} m^{-2}. During deformation, the dislocation density in the BCC phase of the 0 min dwell sample increases slowly to about 3.0×10^{15} m^{-2} at 3% strain.

In the case of the 3 min dwell sample, the dislocation density in the BCC phase also increases slowly when the strain level is below 3% strain. On the other hand, the dislocation density in the FCC phase increases much more rapidly up to a maximum value of 9.0 $\times 10^{15}$ m^{-2} at 6% strain. Interestingly, the dislocation density in the BCC phase of the 3 min dwell sample only slightly exceeds the dislocation density in the 0 min dwell sample after 4% strain. Previous studies have revealed that the martensite phase partially inherits the dislocation structure of the prior austenite grains [74]. Thus, the increase in dislocation density in the BCC phase of the 3 min dwell sample is likely due to the increase in dislocation density of the FCC grains that subsequently undergo a martensitic transformation. Nevertheless, the dislocation density in the BCC phase of both samples saturates at ~3-4$\times$ 10^{15} m^{-2} until necking, which may be rooted in the generally limited dislocation multiplication capability of the martensite.

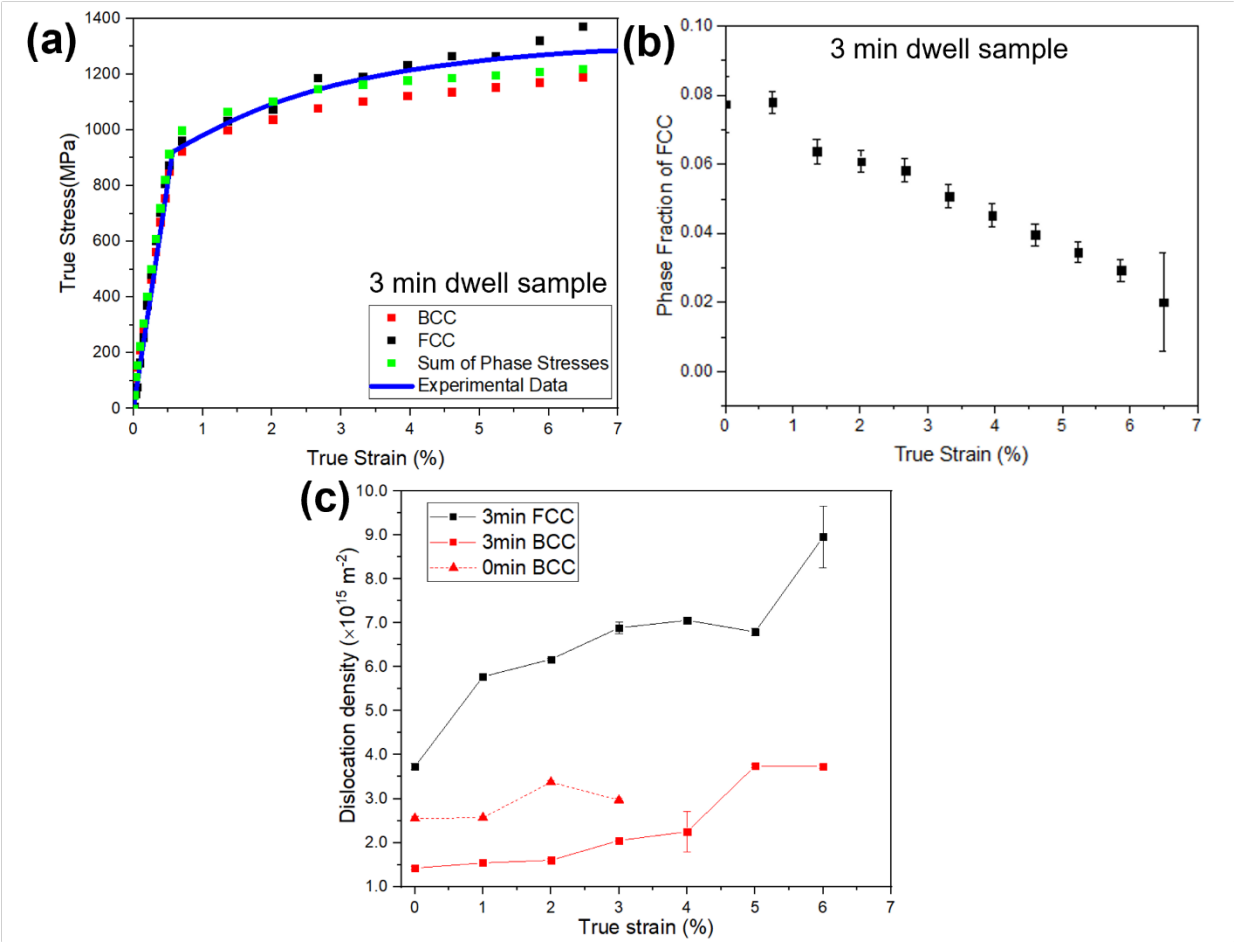

Fig. 11 Deformation mechanism analysis based on the in situ SXRD results. (a) Plot of the estimated stress partitioning between the FCC and BCC phases, the weighted sum of stresses from each phase, and the experimentally measured flow stress in the sample, (b) evolution of the phase fraction of retained austenite during deformation, (c) Dislocation density evolution during deformation.

4.2 Strengthening mechanisms

As previously mentioned, the 3 min dwell sample shows a significant increase in uniform elongation and yield strength compared to the 0 min dwell sample. The increase in uniform elongation arises due to the enhanced work hardening enabled by the stress-induced phase transformation of retained austenite into martensite during deformation, which has been shown to delay the onset of plastic instability (i.e., necking).

It is well known that the yield strength of the FCC austenite phase in maraging steels is often substantially lower than that of the BCC martensite phase [10,55]. As such, it would be reasonable to expect that the inclusion of retained austenite phase would lead to a decrease in the yield strength, but the opposite trend is surprisingly observed in this work. This section presents the theoretical calculations and quantitative estimations of various strengthening mechanisms that result in the different yield strengths between the 0 min and 3 min dwell samples.

In the case of the as-printed maraging 250 steel, there are four main strengthening mechanisms that collectively contribute to the yield strength of the material. These strengthening sources are the lattice friction (σ_f), grain boundary or Hall-Petch strengthening (σ_{HP}), dislocation strengthening (σ_ρ), and solid solution strengthening (σ_{SS}). The yield strength (σ_y) can be estimated as:

$$\sigma_y = \sigma_f + \sigma_{HP} + \sigma_\rho + \sigma_{SS} \quad [3]$$

The lattice friction in maraging steels is approximated as 50 MPa [75]. The Hall-Petch strengthening in maraging steels can be quantified based on the martensite block size (d_{block}) which is analogous to the grain size measured via EBSD [48,57,76] and often correlates with the prior austenite grain (PAG) size [57,75,77]:

$$\sigma_{HP} = \frac{300}{\sqrt{d_{block}}} \quad [4]$$

The value of d_{block} is measured from the EBSD data as 82.6 μm and 15.3 μm for the 0 min and 3 min dwell samples, respectively. The dislocation strengthening is estimated by the Taylor hardening law [78] :

$$\sigma_\rho = M\alpha G b \rho^{1/2} \quad [5]$$

where M is the average Taylor factor measured from EBSD as ~3.0 for both samples. α is a geometric constant that is approximately 0.3. G is the shear modulus calculated from the Young's modulus of each material using the results of the tensile tests (38.1 GPa for the 0 min sample and 63.4 GPa for the 3 min sample). $b \approx 0.25$ nm is the burgers vector. ρ is the dislocation density, which is calculated in the previous section based on the SXRD data. The dislocation strengthening contribution in the 3 min dwell sample is approximated as a weighted sum of the dislocation strengthening in both the austenite and martensite phases. Finally, the solid solution strengthening is estimated based on the Fleischer equation [57,79]:

$$\sigma_{SS} = \sum({\beta_i}^2 x_i)^{1/2} \quad [6]$$

where β_i is the solid solution strengthening constant for the ith solute elements and x_i denotes the atomic fraction of that element. For this work, the β_i constants for the different alloying elements in the maraging 250 steel are extracted from the literature [57]. The solid solution strengthening contribution is approximated as deriving purely from the martensite phase in both samples and yields a similar strengthening effect of ~455 MPa, which is consistent with the prior studies [48].

The combination of the different strengthening mechanisms for both the 3 min and 0 min dwell samples is considered and compared to the experimentally measured yield strengths, as shown in Fig. 12. Notably, the theoretically estimated yield strengths are within 5-7% deviations from the experimentally measured values, which illustrates the accuracy of the previously described strengthening models in predicting the yield strengths of the additively manufactured maraging 250 steels. Given that both the solid solution strengthening, and lattice friction contributions are essentially the same in the 3 min and 0 min dwell samples, it is clear that the enhanced yield strength for the 3 min dwell sample stems from the significantly smaller grain size (Fig. 5) and higher dislocation density (Fig. 11). Both these microstructural features are

achieved via the inclusion of retained FCC austenite that helps to break up the BCC martensite phase, resulting in grain refinement and accommodation of a higher dislocation density in the 3 min dwell sample.

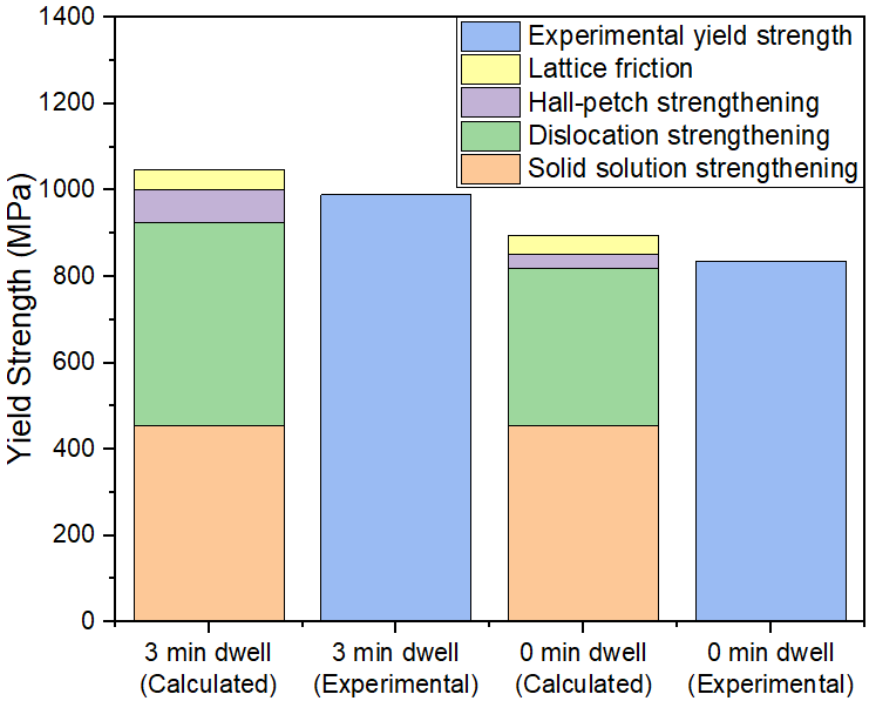

Fig. 12 Theoretically calculated yield strength in comparison to experimentally measured yield strength for different samples.

4.3 Origin of retained austenite formation

The presence of the retained austenite is crucial to the improved mechanical performance of the additively manufactured maraging 250 steel. This section focuses on understanding how the implementation of a dwell time between consecutive layers facilitates the formation of retained austenite. To this end, we first explore the thermal history during printing by finite element thermal modeling of the PAAM process. The temperature distribution in the 0 min and 3 min dwell time samples are illustrated in Fig. 13a and b, respectively. The point of interest (POI) from which the temperature vs time data is extracted is shown in these plots. The POI is positioned in the center of the x-z plane of the first deposited layer as this location represents a point that experiences repeated thermal cycling during the entire printing process and is representative of the thermal history of the bulk material. It is seen that the 0 min dwell sample shows a larger melt pool size than the 3 min dwell sample. Furthermore, the time-temperature curves for the 0 min and 3 min dwell samples are shown in Fig. 13c and d, respectively. The red dotted lines in Fig, 13c, d and the inset of Fig. 13d denote martensite start (M_s) and martensite finish (M_f) temperatures. From Fig. 13c we observe that when no dwell time is permitted between consecutive layers, there is inadequate time to cool the sample to the M_s temperature. Consequently, the material remains a fully austenitic structure during the printing process. After the printing process is completed, the sample is allowed to cool, causing the entire structure to completely undergo the martensitic transformation to form a fully martensite structure. Fig. 13d shows that when a 3 min dwell time is included, the temperature drops to lower temperatures. The inset of Fig. 13d shows a close-up view of the time-temperature profile where it is observed that the temperature at the POI drops below the M_s temperature during the 3 min dwell time, suggesting that the martensitic transformation is activated during cooling. Nonetheless, this POI is then re-heated during

deposition of the next layer before the temperature drops below the M_f temperature, which implies that the martensitic transformation is incomplete. Thus, the austenite and martensite phases co-exist during thermal cycling in the 3 min dwell sample.

The coexistence of the martensite and retained austenite phases allows for elemental partitioning between the dual phases during printing, which can result in stabilization of the retained austenite phase upon cooling down to room temperature. It is well documented that the Ni element redistributes between austenite and martensite phases in maraging steels, enriching the austenite phase in Ni [80]. Ni is a well-known austenite stabilizer that can lower the M_s and M_f temperatures [81] and Ni segregation during AM has been shown to cause austenite stabilization in other steel alloys as well [82]. Recall in Fig. 7 that the austenite in the 3 min dwell samples is rich in Ni compared to the surrounding martensite. The addition of a dwell time results in incomplete martensitic phase transformation such that both the martensite and retained austenite phases are present during the solidification process. Additional thermal cycling during subsequent layer deposition may further induce segregation of the Ni element to the austenite to further stabilize the retained austenite phase upon cooling down to room temperature. It should be noted that in the 0 min dwell sample the thermally driven martensitic transformation does not occur during printing because the temperature does not drop below M_s until after the printing process is completed (see Fig. 13c). Hence, there is no opportunity to redistribute the Ni content to form retained austenite, leading to a fully martensitic structure at room temperature. These results underscore the importance of precisely controlling the thermal history during AM of maraging steels to enable incomplete martensitic transformation and elemental segregation to stabilize the retained austenite upon thermal cycling. In fact, this method of engineering the thermal history by adding a dwell time is unique to the high heating/cooling rates and repeated thermal cycling under AM conditions, where a sample is thermomechanically processed layer by layer. In traditional manufacturing techniques such as casting, the entire part may only experience one thermal cycle and thus requires delicate post-processing protocols to properly tune the microstructure. The introduced thermal history engineering strategy in this work illustrates the unique benefit of AM during which the microstructure and phase transformation pathway of a material can be readily tailored without the need for expensive and time-consuming post-processing procedures.

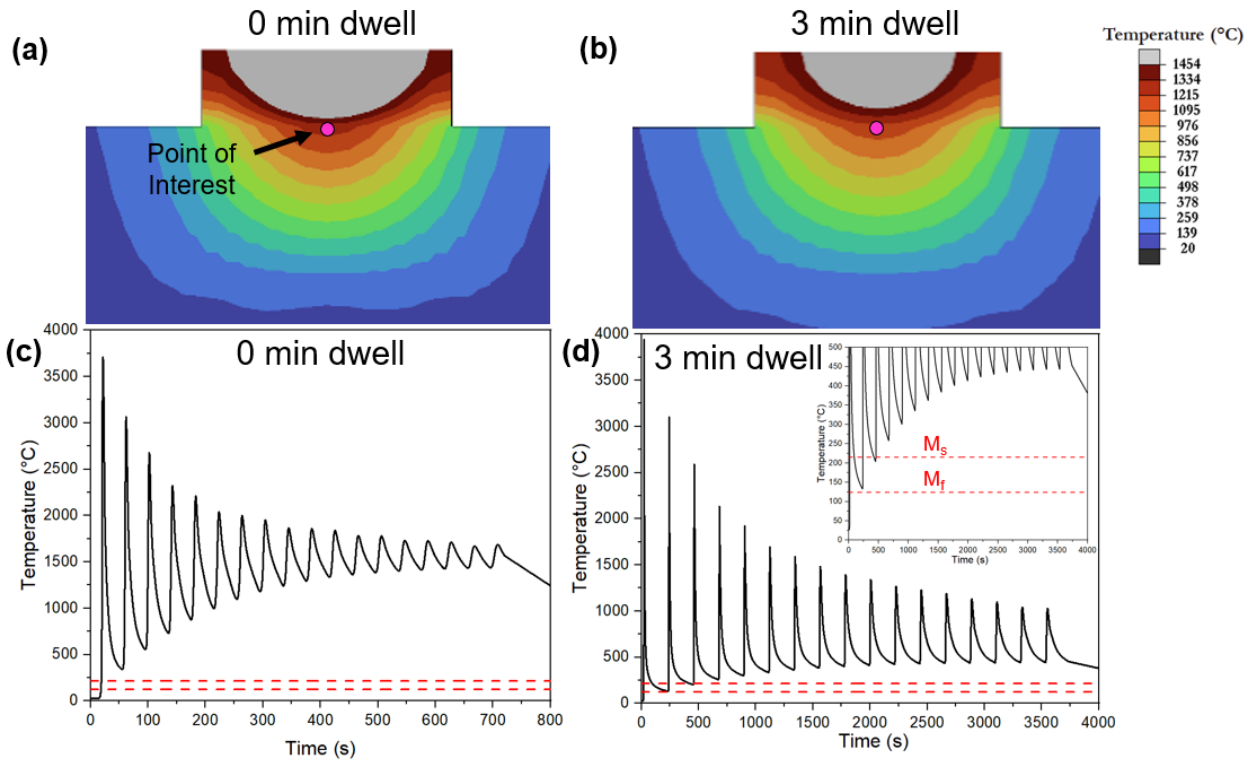

Fig. 13 Simulated time-temperature profiles during printing with 0 min and 3 min dwell times. (a) Temperature distribution in the 0 min dwell time sample. (b) Temperature distribution in the 3 min dwell time sample. (c) Plot of the temperature vs. time profile of the POI in the 0 min dwell sample. (d) Plot of the temperature vs. time profile of the POI in the 3 min dwell sample. The inset of (d) presents a close-up view of the time-temperature profile. The dotted red-lines in (c) and (d) represent the martensite start (M_s) and martensite finish (M_f) temperatures, respectively [48].

5. Conclusions

This study demonstrates the capability of PAAM in controlling the phase and microstructure of maraging steels by strategically engineering the thermal history. By introducing a dwell time between layer depositions, the printed structure undergoes controlled cooling, initiating the martensitic phase transformation while preventing its completion. Subsequent layer depositions and thermal cycling ensure that the temperature of the previous layers remains above the M_f temperature, preserving the coexistence of martensite and austenite phases upon thermal cycling. The controlled thermal history enables the redistribution of crucial alloying elements, such as Ni, from the martensite into the retained austenite phase. This stabilizes the austenite, allowing it to persist when cooling down to room temperature. The retained austenite acts as a barrier to disrupt the epitaxial growth of martensitic grains across layers. Consequently, the printed structure exhibits a weaker texture and smaller martensitic grain size.

With a dwell time between adjacent layers, the cooling rate is elevated, which leads to a higher dislocation density and refined grain size to elevate the yield strength. Furthermore, the retained austenite phase is metastable under loading, a feature that facilitates the stress-induced martensitic transformation during deformation to enhance the overall work hardening and uniform elongation of the additively manufactured maraging 250 steel. The intermittent deposition strategy during PAAM allows us to achieve an outstanding strength-ductility synergy that outperforms conventional wrought and other additively manufactured maraging steel counterparts. By leveraging the high heating/cooling rates as well as the thermal cycling

effect inherent to AM processing, the introduced approach offers a unique opportunity to tailor the phase transformation pathway and microstructure of maraging steels. In summary, our work suggests that engineering the thermal history during AM holds great promise to design novel processing paths for achieving superior mechanical properties in multi-phase alloys with complex microstructures.

CRediT authorship contribution statement

Shahryar Mooraj: Investigation, Formal analysis, Writing – original, Writing – review & editing, Methodology, Visualization. **Shuai Feng:** Investigation, Formal analysis, Writing – review & editing, Methodology. **Matthew Luebbe:** Investigation, Formal analysis, Writing – review & editing. **Matthew Register:** Investigation, Formal analysis, Writing – review & editing. **Tianyi Li:** Investigation. **Baris Yavas:** Investigation, Writing – review & editing. **David P. Schmidt:** Supervision, Writing – review & editing. **Matthew W. Priddy:** Supervision, Writing – review & editing. **Michael B. Nicholas:** Supervision, Funding acquisition. **Victor K. Champagne:** Supervision, Funding acquisition. **Mark Aindow:** Supervision, Writing – review & editing. **Haiming Wen:** Supervision, Writing – review & editing. **Wen Chen:** Supervision, Funding acquisition, Writing – original, Writing – review & editing, Conceptualization.

Declaration of Competing Interest

The authors declare that they have no known competing financial interests or personal relationships that could have appeared to influence the work reported in this paper.

Data availability

Data will be made available on request.

Acknowledgements

W.C. is grateful for the support from the U.S. Army Research Laboratory under Cooperative Agreement Award No. HQ0034-15-2-0007. H.W. acknowledges the support from the U.S. National Science Foundation (DMR-2207965). This research used resources of the Advanced Photon Source, a U.S. Department of Energy (DOE) Office of Science user facility operated for the DOE Office of Science by Argonne National Laboratory under Contract No. DE-AC02-06CH11357. Characterization using the Talos F200X and JEM 2100F was performed at the Center for Nanoscale Materials at Argonne National Laboratory under user proposal 75825. Work performed at the Center for Nanoscale Materials, a U.S. Department of Energy Office of Science User Facility, was supported by the U.S. DOE, Office of Basic Energy Sciences, under Contract No. DE-AC02-06CH11357.

References

[1] T. Simm, L. Sun, D. Galvin, P. Hill, M. Rawson, S. Birosca, E. Gilbert, H. Bhadeshia, K. Perkins, The Effect of a Two-Stage Heat-Treatment on the Microstructural and Mechanical Properties of a Maraging Steel, Materials. 10 (2017) 1346. https://doi.org/10.3390/ma10121346.

[2] Y. Bai, Y. Yang, D. Wang, M. Zhang, Influence mechanism of parameters process and mechanical properties evolution mechanism of maraging steel 300 by selective laser melting, Materials Science and Engineering: A. 703 (2017) 116–123. https://doi.org/10.1016/j.msea.2017.06.033.

[3] K. Kempen, E. Yasa, L. Thijs, J.-P. Kruth, J. Van Humbeeck, Microstructure and mechanical properties of Selective Laser Melted 18Ni-300 steel, Physics Procedia. 12 (2011) 255–263. https://doi.org/10.1016/j.phpro.2011.03.033.

[4] F. Habiby, T.N. Siddiqui, H. Hussain, M.A. Khan, A. ul Haq, A.Q. Khan, Machine-induced phase transformation in a maraging steel, Materials Science and Engineering: A. 159 (1992) 261–265. https://doi.org/10.1016/0921-5093(92)90297-E.
[5] F.F. Conde, J.D. Escobar, J.P. Oliveira, A.L. Jardini, W.W. Bose Filho, J.A. Avila, Austenite reversion kinetics and stability during tempering of an additively manufactured maraging 300 steel, Additive Manufacturing. 29 (2019) 100804. https://doi.org/10.1016/j.addma.2019.100804.
[6] Z. Guo, W. Sha, D. Li, Quantification of phase transformation kinetics of 18 wt.% Ni C250 maraging steel, Materials Science and Engineering: A. 373 (2004) 10–20. https://doi.org/10.1016/j.msea.2004.01.040.
[7] D.P.M. da Fonseca, A.L.M. Feitosa, L.G. de Carvalho, R.L. Plaut, A.F. Padilha, A Short Review on Ultra-High-Strength Maraging Steels and Future Perspectives, Mat. Res. 24 (2021) e20200470. https://doi.org/10.1590/1980-5373-mr-2020-0470.
[8] M.K. Alam, M. Mehdi, R.J. Urbanic, A. Edrisy, Mechanical behavior of additive manufactured AISI 420 martensitic stainless steel, Materials Science and Engineering: A. 773 (2020) 138815. https://doi.org/10.1016/j.msea.2019.138815.
[9] B. Mooney, K.I. Kourousis, R. Raghavendra, D. Agius, Process phenomena influencing the tensile and anisotropic characteristics of additively manufactured maraging steel, Materials Science and Engineering: A. 745 (2019) 115–125. https://doi.org/10.1016/j.msea.2018.12.070.
[10] S.W. Ooi, P. Hill, M. Rawson, H.K.D.H. Bhadeshia, Effect of retained austenite and high temperature Laves phase on the work hardening of an experimental maraging steel, Materials Science and Engineering: A. 564 (2013) 485–492. https://doi.org/10.1016/j.msea.2012.12.016.
[11] K. Ismail, A. Perlade, P.J. Jacques, T. Pardoen, Outstanding cracking resistance of fibrous dual phase steels, Acta Materialia. 207 (2021) 116700. https://doi.org/10.1016/j.actamat.2021.116700.
[12] M. Zhang, X. Zhou, D. Wang, L. He, X. Ye, W. Zhang, Additive manufacturing of in-situ strengthened dual-phase AlCoCuFeNi high-entropy alloy by selective electron beam melting, Journal of Alloys and Compounds. 893 (2022) 162259. https://doi.org/10.1016/j.jallcom.2021.162259.
[13] A.K. Jha, K. Sreekumar, T. Tharian, P.P. Sinha, Process optimization for high fracture toughness of maraging steel rings formed by mandrel forging, Journal of Manufacturing Processes. 12 (2010) 38–44. https://doi.org/10.1016/j.jmapro.2010.01.007.
[14] E. Tekoğlu, A.D. O'Brien, J. Liu, B. Wang, S. Kavak, Y. Zhang, S.Y. Kim, S. Wang, D. Ağaoğulları, W. Chen, A.J. Hart, J. Li, Strengthening additively manufactured Inconel 718 through in-situ formation of nanocarbides and silicides, Additive Manufacturing. 67 (2023) 103478. https://doi.org/10.1016/j.addma.2023.103478.
[15] Y. Liu, J. Ren, S. Guan, C. Li, Y. Zhang, S. Muskeri, Z. Liu, D. Yu, Y. Chen, K. An, Y. Cao, W. Liu, Y. Zhu, W. Chen, S. Mukherjee, T. Zhu, W. Chen, Microstructure and mechanical behavior of additively manufactured CoCrFeMnNi high-entropy alloys: Laser directed energy deposition versus powder bed fusion, Acta Materialia. 250 (2023) 118884. https://doi.org/10.1016/j.actamat.2023.118884.
[16] J. Zhang, B. Song, Q. Wei, D. Bourell, Y. Shi, A review of selective laser melting of aluminum alloys: Processing, microstructure, property and developing trends, Journal of Materials Science & Technology. 35 (2019) 270–284. https://doi.org/10.1016/j.jmst.2018.09.004.
[17] Q. Chen, X. Liang, D. Hayduke, J. Liu, L. Cheng, J. Oskin, R. Whitmore, A.C. To, An inherent strain based multiscale modeling framework for simulating part-scale residual deformation for direct metal laser sintering, Additive Manufacturing. 28 (2019) 406–418. https://doi.org/10.1016/j.addma.2019.05.021.
[18] P. Kürnsteiner, M.B. Wilms, A. Weisheit, B. Gault, E.A. Jägle, D. Raabe, High-strength Damascus steel by additive manufacturing, Nature. 582 (2020) 515–519. https://doi.org/10.1038/s41586-020-2409-3.
[19] J. Ren, Y. Zhang, D. Zhao, Y. Chen, S. Guan, Y. Liu, L. Liu, S. Peng, F. Kong, J.D. Poplawsky, G. Gao, T. Voisin, K. An, Y.M. Wang, K.Y. Xie, T. Zhu, W. Chen, Strong yet ductile nanolamellar

high-entropy alloys by additive manufacturing, Nature. 608 (2022) 62–68. https://doi.org/10.1038/s41586-022-04914-8.
[20] P. Mohammadpour, A. Plotkowski, A.B. Phillion, Revisiting solidification microstructure selection maps in the frame of additive manufacturing, Additive Manufacturing. 31 (2020) 100936. https://doi.org/10.1016/j.addma.2019.100936.
[21] M.H. Farshidianfar, Effect of real-time cooling rate on microstructure in Laser Additive Manufacturing, Journal of Materials Processing Technology. (2016) 11.
[22] S.J. Wolff, Z. Gan, S. Lin, J.L. Bennett, W. Yan, G. Hyatt, K.F. Ehmann, G.J. Wagner, W.K. Liu, J. Cao, Experimentally validated predictions of thermal history and microhardness in laser-deposited Inconel 718 on carbon steel, Additive Manufacturing. 27 (2019) 540–551. https://doi.org/10.1016/j.addma.2019.03.019.
[23] Z. Sun, X. Tan, S.B. Tor, C.K. Chua, Simultaneously enhanced strength and ductility for 3D-printed stainless steel 316L by selective laser melting, NPG Asia Mater. 10 (2018) 127–136. https://doi.org/10.1038/s41427-018-0018-5.
[24] A. Gisario, M. Kazarian, F. Martina, M. Mehrpouya, Metal additive manufacturing in the commercial aviation industry: A review, Journal of Manufacturing Systems. 53 (2019) 124–149. https://doi.org/10.1016/j.jmsy.2019.08.005.
[25] J.J. Lin, Y.H. Lv, Y.X. Liu, B.S. Xu, Z. Sun, Z.G. Li, Y.X. Wu, Microstructural evolution and mechanical properties of Ti-6Al-4V wall deposited by pulsed plasma arc additive manufacturing, Materials & Design. 102 (2016) 30–40. https://doi.org/10.1016/j.matdes.2016.04.018.
[26] P. Hou, S. Mooraj, V.K. Champagne, M.J. Siopis, P.K. Liaw, S. Gerasimidis, W. Chen, Effect of Build Height on Temperature Evolution and Thermally Induced Residual Stresses in Plasma Arc Additively Manufactured Stainless Steel, Metall Mater Trans A. 53 (2022) 627–639. https://doi.org/10.1007/s11661-021-06538-5.
[27] W. Ou, T. Mukherjee, G.L. Knapp, Y. Wei, T. DebRoy, Fusion zone geometries, cooling rates and solidification parameters during wire arc additive manufacturing, International Journal of Heat and Mass Transfer. 127 (2018) 1084–1094. https://doi.org/10.1016/j.ijheatmasstransfer.2018.08.111.
[28] V.T. Le, D.S. Mai, Q.H. Hoang, Effects of cooling conditions on the shape, microstructures, and material properties of SS308L thin walls built by wire arc additive manufacturing, Materials Letters. 280 (2020) 128580. https://doi.org/10.1016/j.matlet.2020.128580.
[29] H.-J. Yi, J.-W. Kim, Y.-L. Kim, S. Shin, Effects of Cooling Rate on the Microstructure and Tensile Properties of Wire-Arc Additive Manufactured Ti–6Al–4V Alloy, Met. Mater. Int. 26 (2020) 1235–1246. https://doi.org/10.1007/s12540-019-00563-1.
[30] W. Xiaowei, Y. Dongqing, H. Yong, Z. Qi, F. Jikang, W. Kehong, Microstructure and Mechanical Properties of As-Deposited and Heat-Treated 18Ni (350) Maraging Steel Fabricated by Gas Metal Arc-Based Wire and Arc Additive Manufacturing, J. of Materi Eng and Perform. 30 (2021) 6972–6981. https://doi.org/10.1007/s11665-021-06102-7.
[31] J. Goldak, A. Chakravarti, M. Bibby, A new finite element model for welding heat sources, Metall Mater Trans B. 15 (1984) 299–305. https://doi.org/10.1007/BF02667333.
[32] J. Ding, Thermo-mechanical Analysis of Wire and Arc Additive Manufacturing Process, (n.d.) 216.
[33] S.H. Lee, CMT-Based Wire Arc Additive Manufacturing Using 316L Stainless Steel: Effect of Heat Accumulation on the Multi-Layer Deposits, Metals. 10 (2020) 278. https://doi.org/10.3390/met10020278.
[34] E.R. Denlinger, J. Irwin, P. Michaleris, Thermomechanical Modeling of Additive Manufacturing Large Parts, Journal of Manufacturing Science and Engineering. 136 (2014). https://doi.org/10.1115/1.4028669.
[35] J.C. Heigel, P. Michaleris, E.W. Reutzel, Thermo-mechanical model development and validation of directed energy deposition additive manufacturing of Ti–6Al–4V, Additive Manufacturing. 5 (2015) 9–19. https://doi.org/10.1016/j.addma.2014.10.003.

[36] F. Montevecchi, G. Venturini, A. Scippa, G. Campatelli, Finite Element Modelling of Wire-arc-additive-manufacturing Process, Procedia CIRP. 55 (2016) 109–114. https://doi.org/10.1016/j.procir.2016.08.024.
[37] X. Jimenez, W. Dong, S. Paul, M.A. Klecka, A.C. To, Residual Stress Modeling with Phase Transformation for Wire Arc Additive Manufacturing of B91 Steel, JOM. 72 (2020) 4178–4186. https://doi.org/10.1007/s11837-020-04424-w.
[38] S. Mooraj, J. Dong, K.Y. Xie, W. Chen, Formation of printing defects and their effects on mechanical properties of additively manufactured metal alloys, Journal of Applied Physics. 132 (2022) 225108. https://doi.org/10.1063/5.0132137.
[39] M.A.L. Phan, D. Fraser, S. Gulizia, Z.W. Chen, Mechanism of hot crack propagation and prevention of crack formation during electron beam powder bed fusion of a difficult-to-weld Co-Cr-Ni-W superalloy, Journal of Materials Processing Technology. 293 (2021) 117088. https://doi.org/10.1016/j.jmatprotec.2021.117088.
[40] W.E. King, H.D. Barth, V.M. Castillo, G.F. Gallegos, J.W. Gibbs, D.E. Hahn, C. Kamath, A.M. Rubenchik, Observation of keyhole-mode laser melting in laser powder-bed fusion additive manufacturing, Journal of Materials Processing Technology. 214 (2014) 2915–2925. https://doi.org/10.1016/j.jmatprotec.2014.06.005.
[41] L. Wang, Y. Zhang, H.Y. Chia, W. Yan, Mechanism of keyhole pore formation in metal additive manufacturing, Npj Comput Mater. 8 (2022) 22. https://doi.org/10.1038/s41524-022-00699-6.
[42] J.V. Gordon, S.P. Narra, R.W. Cunningham, H. Liu, H. Chen, R.M. Suter, J.L. Beuth, A.D. Rollett, Defect structure process maps for laser powder bed fusion additive manufacturing, Additive Manufacturing. 36 (2020) 101552. https://doi.org/10.1016/j.addma.2020.101552.
[43] X.R. Li, Z. Shao, Y.M. Zhang, Double Stage Plasma Arc Pipe Welding Process, (n.d.).
[44] X. Lu, M.V. Li, H. Yang, Comparison of wire-arc and powder-laser additive manufacturing for IN718 superalloy: unified consideration for selecting process parameters based on volumetric energy density, Int J Adv Manuf Technol. 114 (2021) 1517–1531. https://doi.org/10.1007/s00170-021-06990-y.
[45] F. Tariq, R.A. Baloch, B. Ahmed, N. Naz, Investigation into Microstructures of Maraging Steel 250 Weldments and Effect of Post-Weld Heat Treatments, J. of Materi Eng and Perform. 19 (2010) 264–273. https://doi.org/10.1007/s11665-009-9455-1.
[46] B. Wu, Z. Pan, D. Ding, D. Cuiuri, H. Li, J. Xu, J. Norrish, A review of the wire arc additive manufacturing of metals: properties, defects and quality improvement, Journal of Manufacturing Processes. 35 (2018) 127–139. https://doi.org/10.1016/j.jmapro.2018.08.001.
[47] E. Jägle, Z. Sheng, P. Kürnsteiner, S. Ocylok, A. Weisheit, D. Raabe, Comparison of Maraging Steel Micro- and Nanostructure Produced Conventionally and by Laser Additive Manufacturing, Materials. 10 (2016) 8. https://doi.org/10.3390/ma10010008.
[48] K. Jacob, D. Yadav, S. Dixit, A. Hohenwarter, B.N. Jaya, High pressure torsion processing of maraging steel 250: Microstructure and mechanical behaviour evolution, Materials Science and Engineering: A. 802 (2021) 140665. https://doi.org/10.1016/j.msea.2020.140665.
[49] T. Allam, K.G. Pradeep, P. Köhnen, A. Marshal, J.H. Schleifenbaum, C. Haase, Tailoring the nanostructure of laser powder bed fusion additively manufactured maraging steel, Additive Manufacturing. 36 (2020) 101561. https://doi.org/10.1016/j.addma.2020.101561.
[50] P. Liu, Z. Wang, Y. Xiao, M.F. Horstemeyer, X. Cui, L. Chen, Insight into the mechanisms of columnar to equiaxed grain transition during metallic additive manufacturing, Additive Manufacturing. 26 (2019) 22–29. https://doi.org/10.1016/j.addma.2018.12.019.
[51] F. Zhang, M.R. Stoudt, S. Hammadi, C.E. Campbell, E.A. Lass, M.E. Williams, How Austenitic Is a Martensitic Steel Produced by Laser Powder Bed Fusion? A Cautionary Tale, Metals. 11 (2021) 1924. https://doi.org/10.3390/met11121924.
[52] A.J. Knowles, P. Gong, K.M. Rahman, W.M. Rainforth, D. Dye, E.I. Galindo-Nava, Development of Ni-free Mn-stabilised maraging steels using Fe2SiTi precipitates, Acta Materialia. 174 (2019) 260–270. https://doi.org/10.1016/j.actamat.2019.05.034.

[53] K. Jacob, H. Sahasrabuddhe, A. Hohenwarter, S. Dixit, B.N. Jaya, Micro-mechanisms of failure in nano-structured maraging steels characterised through in situ mechanical tests, Nanotechnology. 34 (2023) 025703. https://doi.org/10.1088/1361-6528/ac952d.
[54] X. Xu, S. Ganguly, J. Ding, S. Guo, S. Williams, F. Martina, Microstructural evolution and mechanical properties of maraging steel produced by wire + arc additive manufacture process, Materials Characterization. 143 (2018) 152–162. https://doi.org/10.1016/j.matchar.2017.12.002.
[55] S. Shamsdini, M.H. Ghoncheh, M. Sanjari, H. Pirgazi, B.S. Amirkhiz, L. Kestens, M. Mohammadi, Plastic deformation throughout strain-induced phase transformation in additively manufactured maraging steels, Materials & Design. 198 (2021) 109289. https://doi.org/10.1016/j.matdes.2020.109289.
[56] C. Tan, K. Zhou, W. Ma, P. Zhang, M. Liu, T. Kuang, Microstructural evolution, nanoprecipitation behavior and mechanical properties of selective laser melted high-performance grade 300 maraging steel, Materials & Design. 134 (2017) 23–34. https://doi.org/10.1016/j.matdes.2017.08.026.
[57] X. Mei, Y. Yan, H. Fu, X. Gao, S. Huang, L. Qiao, Effect of aging temperature on microstructure evolution and strengthening behavior of L-PBF 18Ni(300) maraging steel, Additive Manufacturing. 58 (2022) 103071. https://doi.org/10.1016/j.addma.2022.103071.
[58] S. Li, M. Liu, Y. Ren, Y. Wang, Hydrogen embrittlement behaviors of additive manufactured maraging steel investigated by in situ high-energy X-ray diffraction, Materials Science and Engineering: A. 766 (2019) 138341. https://doi.org/10.1016/j.msea.2019.138341.
[59] T. Bhardwaj, M. Shukla, Effect of laser scanning strategies on texture, physical and mechanical properties of laser sintered maraging steel, Materials Science and Engineering: A. 734 (2018) 102–109. https://doi.org/10.1016/j.msea.2018.07.089.
[60] S. Dehgahi, M.H. Ghoncheh, A. Hadadzadeh, M. Sanjari, B.S. Amirkhiz, M. Mohammadi, The role of titanium on the microstructure and mechanical properties of additively manufactured C300 maraging steels, Materials & Design. 194 (2020) 108965. https://doi.org/10.1016/j.matdes.2020.108965.
[61] P.L.L. Santos, J.A. Avila, E.B. Da Fonseca, A.H.G. Gabriel, A.L. Jardini, É.S.N. Lopes, Plane-strain fracture toughness of thin additively manufactured maraging steel samples, Additive Manufacturing. 49 (2022) 102509. https://doi.org/10.1016/j.addma.2021.102509.
[62] G. Casalino, S.L. Campanelli, N. Contuzzi, A.D. Ludovico, Experimental investigation and statistical optimisation of the selective laser melting process of a maraging steel, Optics & Laser Technology. 65 (2015) 151–158. https://doi.org/10.1016/j.optlastec.2014.07.021.
[63] H.M. Ledbetter, M.W. Austin, Elastic constant versus temperature behavior of three hardened maraging steels, Materials Science and Engineering. 72 (1985) 65–69. https://doi.org/10.1016/0025-5416(85)90067-9.
[64] T. Childerhouse, M. Jackson, Near Net Shape Manufacture of Titanium Alloy Components from Powder and Wire: A Review of State-of-the-Art Process Routes, Metals. 9 (2019) 689. https://doi.org/10.3390/met9060689.
[65] Z. Cheng, S. Sun, X. Du, Q. Tang, J. Shi, X. Liu, Q. Jianrong, Microstructural evolution of a FeCo15Cr14Ni4Mo3 maraging steel with high ductility prepared by selective laser melting, Materials Today Communications. 31 (2022) 103243. https://doi.org/10.1016/j.mtcomm.2022.103243.
[66] S. Feng, S. Guan, S. Zhang, S. Mooraj, M. Luebbe, X. Fan, K.A. Beyer, T. Li, J. Liu, J. Kong, P.K. Liaw, H. Wen, S. Gerasimidis, W. Chen, Ultrafine-grained Fe-TiB2 high-modulus nanocomposite steel with high strength and isotropic mechanical properties by laser powder bed fusion, Additive Manufacturing. 70 (2023) 103569. https://doi.org/10.1016/j.addma.2023.103569.
[67] Y.M. Wang, T. Voisin, J.T. McKeown, J. Ye, N.P. Calta, Z. Li, Z. Zeng, Y. Zhang, W. Chen, T.T. Roehling, R.T. Ott, M.K. Santala, P.J. Depond, M.J. Matthews, A.V. Hamza, T. Zhu, Additively manufactured hierarchical stainless steels with high strength and ductility, Nature Mater. 17 (2018) 63–71. https://doi.org/10.1038/nmat5021.

[68] W. Chen, T. Voisin, Y. Zhang, J.-B. Florien, C.M. Spadaccini, D.L. McDowell, T. Zhu, Y.M. Wang, Microscale residual stresses in additively manufactured stainless steel, Nat Commun. 10 (2019) 4338. https://doi.org/10.1038/s41467-019-12265-8.
[69] D. Yu, L. Huang, Y. Chen, P. Komolwit, K. An, Real-Time In Situ Neutron Diffraction Investigation of Phase-Specific Load Sharing in a Cold-Rolled TRIP Sheet Steel, JOM. 70 (2018) 1576–1586. https://doi.org/10.1007/s11837-018-2947-4.
[70] X.X. Zhang, A. Lutz, H. Andrä, M. Lahres, W.M. Gan, E. Maawad, C. Emmelmann, Evolution of microscopic strains, stresses, and dislocation density during in-situ tensile loading of additively manufactured AlSi10Mg alloy, International Journal of Plasticity. 139 (2021) 102946. https://doi.org/10.1016/j.ijplas.2021.102946.
[71] L. Ma, L. Wang, Z. Nie, F. Wang, Y. Xue, J. Zhou, T. Cao, Y. Wang, Y. Ren, Reversible deformation-induced martensitic transformation in Al0.6CoCrFeNi high-entropy alloy investigated by in situ synchrotron-based high-energy X-ray diffraction, Acta Materialia. 128 (2017) 12–21. https://doi.org/10.1016/j.actamat.2017.02.014.
[72] X.X. Zhang, A. Lutz, H. Andrä, M. Lahres, W.M. Gan, E. Maawad, C. Emmelmann, Evolution of microscopic strains, stresses, and dislocation density during in-situ tensile loading of additively manufactured AlSi10Mg alloy, International Journal of Plasticity. 139 (2021) 102946. https://doi.org/10.1016/j.ijplas.2021.102946.
[73] F. HajyAkbary, J. Sietsma, A.J. Böttger, M.J. Santofimia, An improved X-ray diffraction analysis method to characterize dislocation density in lath martensitic structures, Materials Science and Engineering: A. 639 (2015) 208–218. https://doi.org/10.1016/j.msea.2015.05.003.
[74] J. Macchi, S. Gaudez, G. Geandier, J. Teixeira, S. Denis, F. Bonnet, S.Y.P. Allain, Dislocation densities in a low-carbon steel during martensite transformation determined by in situ high energy X-Ray diffraction, Materials Science and Engineering: A. 800 (2021) 140249. https://doi.org/10.1016/j.msea.2020.140249.
[75] E.I. Galindo-Nava, P.E.J. Rivera-Díaz-del-Castillo, A model for the microstructure behaviour and strength evolution in lath martensite, Acta Materialia. 98 (2015) 81–93. https://doi.org/10.1016/j.actamat.2015.07.018.
[76] Y. Xu, B. Mishra, S.P. Narra, Experimental investigation of in-situ microstructural transformations in wire arc additively manufactured maraging 250-grade steel, Materials Characterization. 190 (2022) 112065. https://doi.org/10.1016/j.matchar.2022.112065.
[77] J. Hidalgo, M.J. Santofimia, Effect of Prior Austenite Grain Size Refinement by Thermal Cycling on the Microstructural Features of As-Quenched Lath Martensite, Metall Mater Trans A. 47 (2016) 5288–5301. https://doi.org/10.1007/s11661-016-3525-4.
[78] Y. Zou, H. Ma, R. Spolenak, Ultrastrong ductile and stable high-entropy alloys at small scales, Nat Commun. 6 (2015) 7748. https://doi.org/10.1038/ncomms8748.
[79] E.I. Galindo-Nava, W.M. Rainforth, P.E.J. Rivera-Díaz-del-Castillo, Predicting microstructure and strength of maraging steels: Elemental optimisation, Acta Materialia. 117 (2016) 270–285. https://doi.org/10.1016/j.actamat.2016.07.020.
[80] W. Zhou, H. Guo, Z. Xie, X. Wang, C. Shang, High strength low-carbon alloyed steel with good ductility by combining the retained austenite and nano-sized precipitates, Materials Science and Engineering: A. 587 (2013) 365–371. https://doi.org/10.1016/j.msea.2013.06.022.
[81] P. Kürnsteiner, M.B. Wilms, A. Weisheit, P. Barriobero-Vila, E.A. Jägle, D. Raabe, Massive nanoprecipitation in an Fe-19Ni-xAl maraging steel triggered by the intrinsic heat treatment during laser metal deposition, Acta Materialia. 129 (2017) 52–60. https://doi.org/10.1016/j.actamat.2017.02.069.
[82] S. Cheruvathur, E.A. Lass, C.E. Campbell, Additive Manufacturing of 17-4 PH Stainless Steel: Post-processing Heat Treatment to Achieve Uniform Reproducible Microstructure, JOM. 68 (2016) 930–942. https://doi.org/10.1007/s11837-015-1754-4.